Numerical simulation of the flow field over conical, disc and flat spiked body at Mach 6

R. C. Mehta
drrakhab.mehta@gmail.com
Nanyang Technological University
Singapore

ABSTRACT

A forward facing spike attached to a hemispherical body significantly changes its flow field and influences aerodynamic drag and wall heat flux in a high speed flow. The dynamic pressure in the recirculation area is highly reduced and this leads to the decrease in the aerodynamic drag and heat load on the surface. Consequently, the geometry, that is, the length and shape of the spike, has to be simulated in order to obtain a large conical recirculation region in front of the blunt body to get beneficial drag reduction. It is, therefore, a potential candidate for aerodynamic drag reduction for a future high speed vehicle. Axisymmetric compressible laminar Navier-Stokes equations are solved using a finite volume discretisation in conjunction with a multistage Runge-Kutta time stepping scheme. The effect of the spike length and shape, and the spike nose configuration on the reduction of drag is numerically evaluated at Mach 6 at a zero angle-of-attack. The computed density contours agree well with the schlieren images. Additional modification to the tip of the spike to get different types of flow field such as the formation of a shock wave, separation area and reattachment point are examined. The spike geometries include the conical spike, the flat-disk spike and the hemispherical disk spike of different length to diameter ratios attached to the blunt body.

NOMENCLATURE

C_f	skin friction coefficient
C_p	specific heat at constant pressure
D	diameter of the blunt body, m
e	specific energy, J/kg
F, G	inviscid flux vectors
H	source vector
M	Mach number
Pr	Prandtl number
p	static pressure, Pa
q	heat flux, W/m^2
R	radius of the blunt body, m
R, S	viscous vectors
T	temperature, K
t	time, s
u, v	velocity components, ms^{-1}
W	conservative variables in vector form
x, r	coordinate directions, m
γ	ratio of specific heats
μ	molecular viscosity, kg/m.s
ρ	density, kg/m^3
σ	normal stress, N/m^2
τ	shear stress, N/m^2

1.0 INTRODUCTION

A high-speed flow past a blunt body generates a bow shock wave which causes high surface pressure and as a result the development of high aerodynamic drags. The dynamic pressure on the surface of the blunt body can be substantially reduced by creating a low pressure region in front of the blunt body by mounting a spike. The use of the forward facing spike attached with the shape of a hemispherical blunt body appears to be most effective and simple method to integrate the vehicle as compared with the focused energy depostion[1] and telescopic aerodisk[2]. A blunt body creates a bow shock wave at high Mach number, which produces a very high pressure in the forward region of the hemispherical region, which leads to an increase of high wave drag during the projectile's flight through the atmosphere. It is advantageous to have a vehicle with a low drag coefficient in order to minimise the thrust required from the propulsive system during the supersonic and hypersonic regime. There will be a trade-off study between the thermal protection system and high wave drag associated with shock wave formation on such high speed vehicles. Aerospike, energy deposition along the stagnation streamline, the forward facing jet in the stagnation pressure zone of a blunt body and the artificial blunted nose cone-out are studied numerically and experimentally to access the capability to reduce the aerodynamic drag and the wall heat flux. Many researchers have investigated the flow field simulations over the blunt body attached with forward facing aerospike.

The experimental investigations of the flow field characteristics around the spiked-blunt body at high speed have been initiated since late 1940s. The prime concern has been with regard to drag characteristics where effects due to spike length, spike head geometry, forward body geometry and relative spike diameter have been explored. Most of the experimental studies on spiked bodies are carried out to get effects on aerodynamic heating[3-5] and the surface pressure distributions[6-8] at supersonic and hypersonic Mach numbers[9-12]. Kubota[13] has experimentally investigated the overall characteristics of the spiked blunt body configuration at hypersonic Mach numbers. Crawford[14] experimentally investigated the effects of the spike length on the nature of the flow field for a freestream Mach number 6·8 and Reynolds number $0·12 \times 10^6 - 1·5 \times 10^6$ based on the cylinder diameter. The spike drastically influences the aerodynamic drag of the blunted body at high-speeds. However, because of the reattachment of the shear layer on the shoulder of the hemispherical body, the pressure near that reattachment point becomes large. Motoyama et al[15] have experimentally investigated the aerodynamic and heat transfer characteristics of conical, hemispherical, flat-faced aerospike, and hemispherical and flat-faced disk attached to the aerospike for a freestream Mach number 7, freestream Reynolds number 4×10^5/m, for L/D = 0·5 and 1·0, and angle-of-attack 0 to 8 deg, where L is the spike length and D is the diameter of the blunt body. They found that the aerodisk spike (L/D = 1·0 and aerodisk diameter of 10mm), has a superior drag reduction capability as compared to the other aerospikes. Yamauchi et al[16] have numerically investigated the flow field around a spiked blunt body at freestream mach numbers of 2·01, 4·14 and 6·80 for different ratio of L/D. Shoemaker[17], Fujita and Kubota[18], Kamaran et al[19] used a numerical approach to solve the compressible Navier-Stokes equations. The reattachment point can be moved backward or removed, which depends on the spike length or the nose configuration. However, because of the reattachment of the shear layer on the shoulder of the hemispherical body, the pressure near that point becomes large. Milicev et al[20] have experimentally investigated the influence of four different types of spikes attached to a hemisphere-cylinder body at Mach number 1·89, Reynolds number $0·38 \times 10^6$ based on the cylinder diameter, and at an angle-of-attack 2°deg. They observed in their experimental studies that a reliable estimation of the aerodynamic effects of the spike can be made in conjunction with flow visualisation technique. Numerical simulations[21-23] have been carried out to get the comparative studies of the flowfield over

the spike. Peak heating for the reattachment of the separated flow on a spiked blunt body is numerically studied for freestream Mach numbers 2·01, 4·15 and 6·80. Recently, the axisymmetric numerical simulation[24] has been performed for different types of spikes attached to a blunt nose cone at Mach numbers of 5·0, 7·0 and 10·0 employing CFD-FASTRAN flow solver.

A schematic of the flow field over the aerodisk and the conical spiked blunt body at zero angle-of-attack is delineated in Fig. 1(a) and (b), respectively. A typical flow over a spike attached to a blunt body is based on experimental investigations. The flow field around a spiked blunt body appears to be very complicated and complex and contains a number of interesting flow phenomena and characteristic, which has yet to be investigated. The high speed flow past the aero-hemispherical spike shows a formation of a bow shock wave which remains away from the spike as illustrated in Fig. 1(a). In the case of the conical spike, the flow field characterised by a conical shock wave emanating from the tip of the spike as depicted in Fig. 1(b). The recirculating region is formed around the root of the spike up to the reattachment point of the flow at the shoulder of the hemispherical body. A recirculation flow region is a function of the geometrical parameters of the spike. The reattachment shock wave on the shoulder of the blunt body increases the local surface pressure and wall heat flux. The ratio of the spike length to spike diameter influences the drag reduction mechanism. This flow field has also been numerically investigated and physical aspects of the flow field have been described in the present analysis. The main aim of the present study is to numerically investigate the flow field behavior and to calculate surface pressure, skin friction coefficient and wall heat flux distributions and aerodynamic drag over the forward facing spike of various shape and size at Mach number 6. The present paper presents a numerical simulation of the flow field over an aero-disc spike and a conical spike carried out for different L/D ratios. The focus of the present numerical analysis to investigate the mechanism of drag reduction and flow field pattern at a freestream Mach number 6 and L/D ratio of 0·5, 1·0, 1·5 and 2·0. However, the flow fields around the aero-hemispherical disc and the aero flat-face disc spiked attached to the blunt body have not been computed previously at freestream Mach number 6. The flow field features captured by the density, Mach and pressure contours are used to understand the mechanism of the drag reduction. The influence of the spike shock wave generated from the spike, interacting with the reattachment shock is also studied, to understand the cause of drag reduction.

2.0 GOVERNING FLUID DYNAMICS EQUATIONS

Experimental data obtained from the wind-tunnel tests at a zero angle-of-attack show that the flow pattern remains the same with reference to the tunnel configuration. Measurements made from two diametrically opposite locations indicate that the flow is axisymmetric. A numerical simulation of the unsteady, compressible, laminar, axisymmetric Navier-Stokes equations is attempted in order to understand the basic fluid dynamics over the spiked blunt body. The governing equations can be written in the following strong conservation form

$$\frac{\partial \mathbf{W}}{\partial t} + \frac{\partial \mathbf{F}}{\partial x} + \frac{\partial \mathbf{G}}{\partial r} + \mathbf{H} = \left[\frac{\partial \mathbf{R}}{\partial x} + \frac{\partial \mathbf{S}}{\partial r} \right] \qquad \ldots (1)$$

where $\mathbf{W}$ is conservative state vector, and $\mathbf{F}$ and $\mathbf{G}$ are inviscid flux vectors and expressed as

$$\mathbf{R} = r \begin{bmatrix} 0 \\ \sigma_{xx} \\ \tau_{xr} \\ u\sigma_{xx} + v\tau_{xr} + q_x \end{bmatrix}, \quad \mathbf{S} = r \begin{bmatrix} 0 \\ \tau_{xx} \\ \sigma_{xr} \\ u\tau_{xr} + v\sigma_{rr} + q_r \end{bmatrix}, \quad \mathbf{H} = \begin{bmatrix} 0 \\ 0 \\ \sigma_+ \\ 0 \end{bmatrix} \qquad \ldots (2)$$
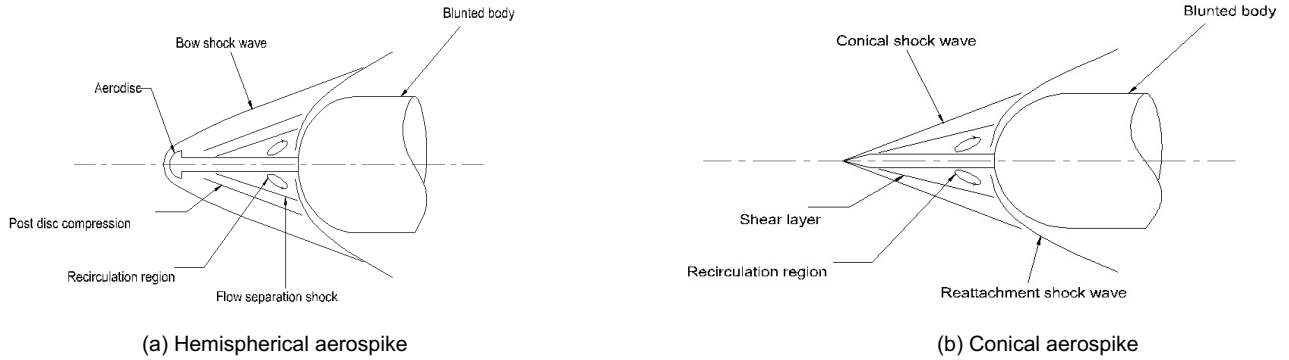
Figure 1. Schematic sketch of the flow field over aerospike.

(a) Hemispherical aerospike

(b) Conical aerospike

(a) Flat-disk spike

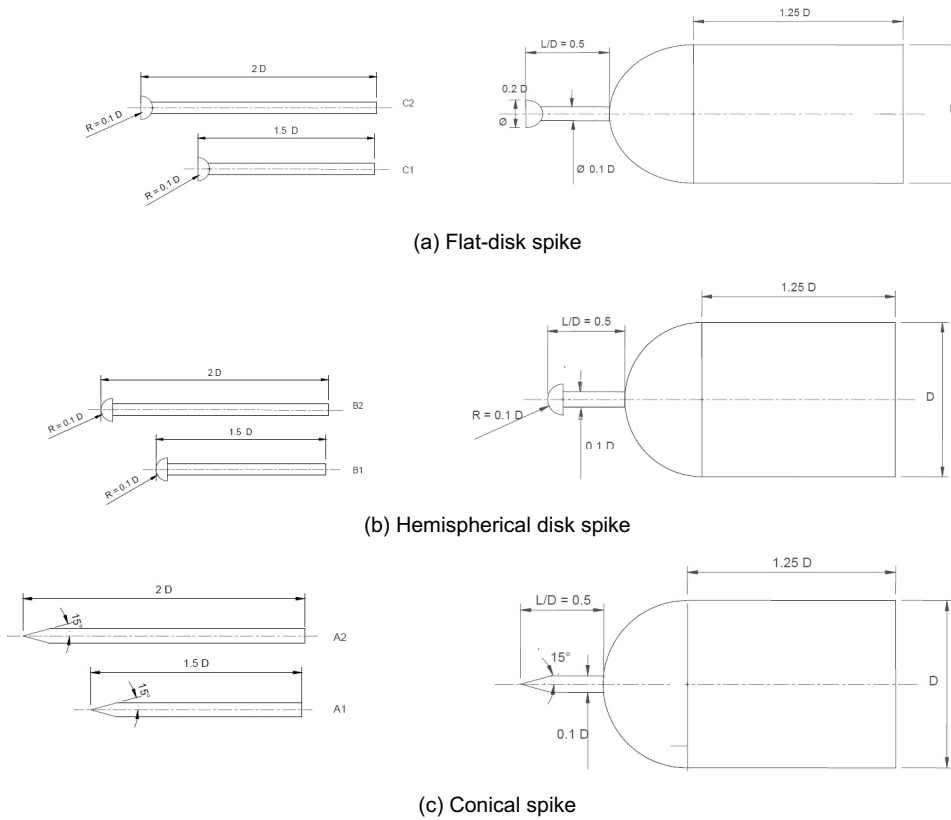(b) Hemispherical disk spike

(c) Conical spike

Figure 2. Dimensions of flat-disk, hemispherical, and conical spike configurations.

and the **R** and **S** viscous flux vectors and **H** are the source vector and written as

$$\mathbf{R} = r \begin{bmatrix} 0 \\ \sigma_{xx} \\ \tau_{xr} \\ u\sigma_{xx} + v\tau_{xr} + q_x \end{bmatrix}, \quad \mathbf{S} = r \begin{bmatrix} 0 \\ \tau_{xx} \\ \sigma_{xr} \\ u\tau_{xr} + v\sigma_{rr} + q_r \end{bmatrix}, \quad \mathbf{H} = \begin{bmatrix} 0 \\ 0 \\ \sigma_+ \\ 0 \end{bmatrix} \quad \dots (3)$$

where σ_{xx}, σ_{rr}, τ_{xr}, and σ_+ are the components of the stress vector and q_x and q_r are the component of the heat flux vector, u and v are the axial- and radial- velocity components in the x and r direction, respectively, and e is the specific energy. The viscous and heat flux terms in the equations became

$$\sigma_{xx} = -\frac{2}{3}\mu\nabla\cdot U + 2\mu\frac{\partial u}{\partial x}$$

$$\sigma_{rr} = -\frac{2}{3}\mu\nabla\cdot U + 2\mu\frac{\partial v}{\partial r}$$

$$\tau_{xr} = \mu\left(\frac{\partial u}{\partial r} + \frac{\partial v}{\partial x}\right)$$

$$\sigma_+ = -p - \mu\frac{2}{3}\nabla\cdot U + 2\mu\frac{v}{r}$$

$$\nabla\cdot U = \frac{\partial u}{\partial x} + \frac{\partial v}{\partial r} + \frac{v}{r}$$

$$q_x = -\frac{C_P\mu}{\text{Pr}}\frac{\partial T}{\partial x}$$

$$q_r = -\frac{C_P\mu}{\text{Pr}}\frac{\partial T}{\partial r} \qquad \dots (4)$$

where C_P is specific heat at constant pressure, U is the mean stream velocity, Pr is Prandtl number and is taken a constant value of 0.72. The coefficient of molecular viscosity μ is calculated according to Sutherland's law

$$\mu = 1.458 \times 10^{-6} \frac{T^{1.5}}{T + 110.4} \qquad \ldots (5)$$

The temperature T is related to pressure p and density ρ by perfect gas equation of state as;

$$\frac{p}{(\gamma - 1)\rho} = \left[e - \frac{1}{2}\left(u^2 + v^2\right) \right] \qquad \ldots (6)$$

The ratio of the specific heats γ is assumed constant and is equal to 1.4. The flow is assumed to be laminar, which is also consistent to Bogdonoff and Vas[3], Yamauchi *et al*[16], Fujita and Kubota[18], and Boyce *et at*[19].

3.0 NUMERICAL SCHEME

To facilitate the spatial discretisation in the numerical simulation, the governing fluid mechanics Equation (1) is written in integral form of a finite volume of the computational domain. The spatial and temporal terms are decoupled using the method of lines. The spatial computation domain was divided into a finite number of non-overlapping quadrilateral cells. Thus, the discretised solution to the governing equations results in a set of volume-averaged state variables for mass, momentum, and energy, which are in balance with their area-averaged fluxes (inviscid and viscous) across the cell faces[25]. The finite code constructed in this manner reduces to a central difference scheme and is second-order accurate in space provided that the mesh is smooth enough. The cell-centered spatial discretisation scheme is non-dissipative; therefore, artificial dissipation terms are included as a blend of a Laplacian and biharmonic operator in a manner analogous to the second and fourth difference. The artificial dissipation terms was added explicitly to prevent numerical oscillations near the shock waves to damp high-frequency modes. Temporal integration was performed using the three-stage time-stepping scheme of Jameson *et al*[26] based on the Runge-Kutta method. The artificial dissipation is evaluated only on first stage and then frozen for the subsequent stages. A conservative choice of the Courant-friedrichs-Lewy (CFL) number is taken as 1.4 in order to achieve stable numerical solution. The details of this flow field technique are further described in Ref. 27. The solver uses a time-marching procedure to compute the flow. The flow is defined to be steady because the flowfield is converging to a steady state. The steady options use local time stepping, which leads to a faster convergence to the steady-state flow field.

3.1 Initial and boundary conditions

Conditions corresponding to a freestream Mach number 6.0 are given as initial conditions. All the variables were extrapolated at the outer boundary, and the no-slip wall condition was used to implement the boundary conditions. An isothermal condition was prescribed for the surface of the model, that is, a wall temperature of 300K. The symmetric condition is applied on the centerline.

4.0 MODEL AND GRID GENERATION

4.1 Spike geometry

The dimensions of the spiked blunt body considered in the present analysis are shown in Fig. 2. The model is axisymmetric, the main body has a hemispherical-cylinder nose, and diameter D is 4.0×10^{-2} m. The spike consists of an aerodisc part and a cylindrical part. The diameter of the cylinder of the spike is $0.1D$. Spike having a hemispherical cap of radius $0.1D$ attached to a stem of diameter of $0.1D$. The aerodisk type spike configuration utilises a disk on its nose of radius $0.1D$ as shown in Fig. 2(a). The radius of the aerodisk is $0.01D$. The diameter of the aerodisk attached to the spike is twice that of the diameter of the spike-stem. Figure 2(b) shows the hemisphere aerodisk with spike lengths $L = 0.5D$, $1.5D$ and $2.0D$. The spike consists of a conical part and a cylindrical part as shown in Fig. 2(c). The diameter of the cylinder of the spike is $0.1D$. The angle of the cone is 15 deg for the conical spike as depicted in Fig. 2(c). The spike model has a simple stick configuration. The spike lengths $L = 0.5D$, $1.0D$, $1.5D$ and $2.0D$ are simulated numerically.

4.2 Computational grid generation

One of the controlling factors for the numerical simulation is the proper grid arrangement. The grid points are generated by a homotopy scheme[28] in conjunction with finite element method[29]. The spiked blunt body is defined by a number of grid points in the cylindrical coordinate system. Using these surface points as the reference nodes, the normal coordinate is then described by the exponentially structured field points, $(x_{i,j}, r_{i,j})$ extending outwards up to an outer computational boundary. Sufficient grid points are allotted in the shoulder region of the spike. The stretching of grid points in the normal direction is obtained using the following expression

$$x_{i,j} = x_{i,0}\left[\frac{e^{\frac{(j-1)\beta}{nr-1}} - 1}{e^{\beta} - 1} \right] + x_{i,w}\left[\frac{e^{\frac{(j-1)\beta}{nr-1}} - 1}{e^{\beta} - 1} \right] \qquad \ldots (7)$$

$$r_{i,j} = r_{i,0}\left[\frac{e^{\frac{(j-1)\beta}{nr-1}} - 1}{e^{\beta} - 1} \right] + r_{i,w}\left[\frac{e^{\frac{(j-1)\beta}{nr-1}} - 1}{e^{\beta} - 1} \right] \quad \begin{array}{l} I = 1, 2, 3, \ldots, nx \\ j = 1, 2, 3, \ldots, nr \end{array}$$

where $r_{i,w}$ and $r_{i,0}$ are the wall and outer surface points, respectively, and β is a stretching factor. nx and nr are the total number of grid points in the x and r directions, respectively. Grid independent tests[30] were carried out, taking into consideration the effect of the computational domain, the stretching factor to control the grid intensity near the wall, and the number of grid points in the axial and normal directions. The outer boundary of the computational domain is varied from 2.5 to 3.0 times the blunt body diameter D and the grid-stretching factor in the radial direction is varied from 1.5 to 5. These stretched grids are generated in an orderly manner. To verify the chosen grid delivers an accurate solution, the number of grid cells was increased until a steady state solution occurred, that is, the resulting axial force on the investigated shape did not change anymore. Several test runs were made with a total doubled grid cell number. Therefore, the grid was highly refined in both directions. Grids are chosen with the number of grid points in the i direction ranging from 187 for the shortest blunt spike to 220 for the longest spike configuration, and the number in the j direction ranging from 52 to 82. The present numerical analysis was performed on 187×62 grid points. The downstream boundary of the computational domain is maintained at 4 to 6 times the blunt body diameter D. This grid
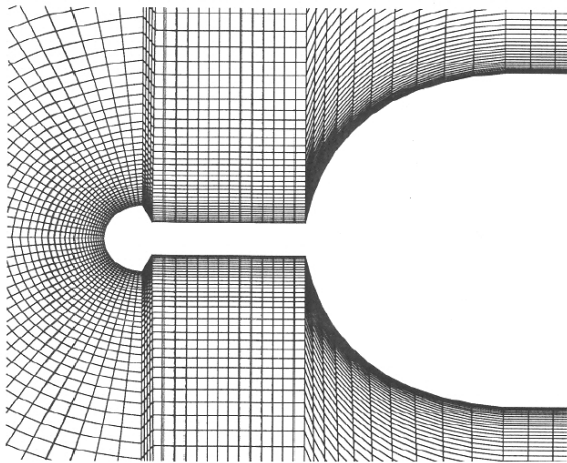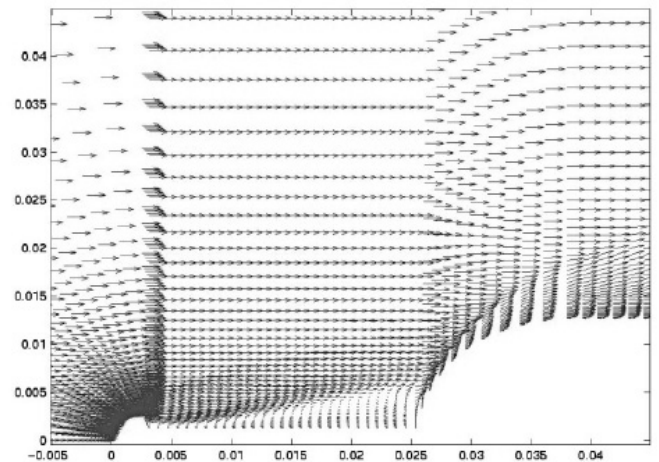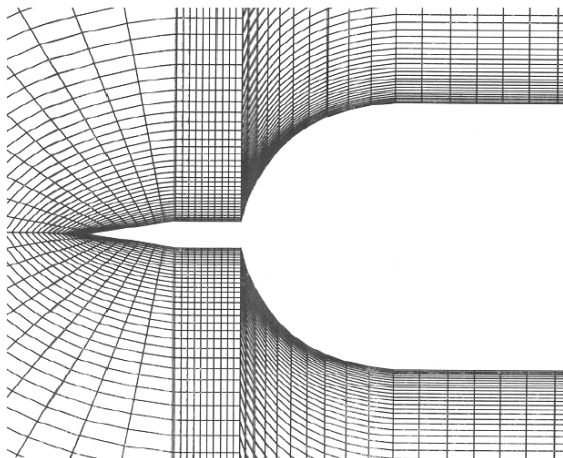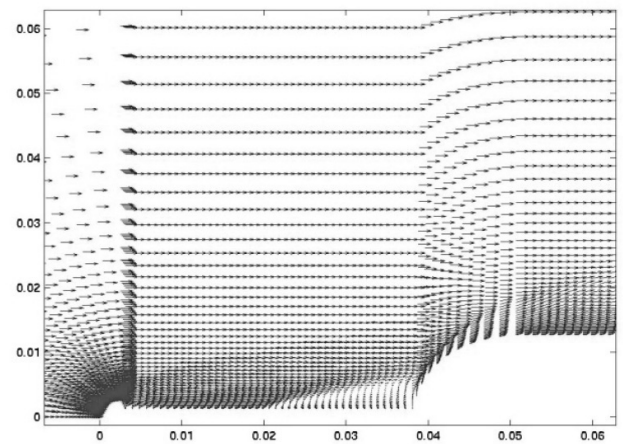
Hemispherical disk space
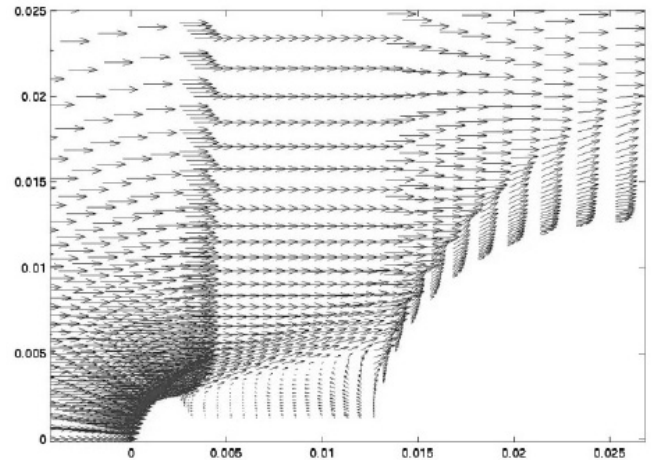
L/D = 0·5
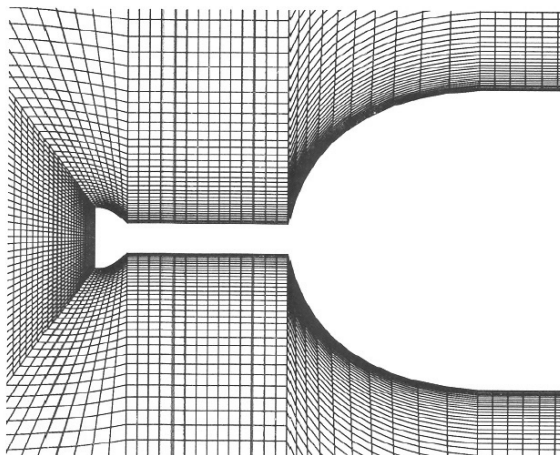
Flat-disk spike

L/D = 1·0

Conical spike

L/D = 2·0

Figure 3. Enlarged view of grid.

Figure 4. Velocity vector for hemispherical spike.

arrangement is found to give a relative difference of about ±1·5% for the drag coefficient. The convergence criterion less than the 10^{-5} is based on the difference in the density values at any grid point between two successive iterations. The minimum spacing for the fine mesh is dependent upon the Reynolds number and is calculated by $\Delta r = (\frac{2}{3})D\sqrt{\mathrm{Re}_D}$. The finer mesh near the wall helps to resolve the viscous effects. The coarse-mesh helps reducing the computer time. A close-up view of the computational grid over the hemispherical, the conical, and the flat-faced aerospike is shown in Fig. 3. The structured grid generation and the mono block is suitable to accommodate spike shape. As seen in the figures, these types of grid use quadrilateral cells in 2-Dimensional in the computational array. The quadrilateral cells, which are very efficient at filling space, support a high amount of skew and stretching before the solution will be significantly affected. Additionally, the grid can be aligned with the flow, thereby yielding greater accuracy within the solver.

5.0 RESULTS AND DISCUSSION

The above mentioned numerical algorithm is applied to obtain the flow field over the hemispherical disk, the flat-face disk and the conical spike attached to the hemispherical blunt body. The current experimental data consists of schlieren pictures and aerodynamic drag at freestream Mach number 6 for the comparison purposes.

5.1 Flow field visualisation and characteristics

Figures 4-6 depict the velocity vector plots over the hemispherical aerospike, the flat-disk aerospike and the conical spike for the L/D ratio of 0·5, 1·0, and 2·0 at freestream Mach number 6. Characteristic behaviours of the flow field around the spiked-blunt body at supersonic speeds are investigated with the help of velocity vector, density, pressure and Mach contours plots. The bow shock wave follows the aerospike contour and the fore-body is entirely subsonic up to the corner tangency point of the flat-faced aerospike and the hemispherical aerospike where the sonic line is located. The effects of the sonic line on the aerodynamic design parameters have been investigated[31,32]. A low pressure is formed immediately downstream of the base which is characterised by a low speed recirculating flow region. It can be attributed to the filling up of the growing space between the shock wave and the body. In Fig. 6, interaction between the conical oblique shock wave starting from the tip of the spike and the reattachment shock wave of the blunt body can be visualised. The reflected reattachment wave and the shear layer from the interaction are seen behind the reattachment shock wave. A large separated region is observed in front of the blunt body and the shear layer; and the boundary of the separated region is clearly observed in Figs 4-6. The separation zone depends on the shape of the spike and L/D ratio. A strong recirculating flow at the spike can be observed distinctly. The effect of spike length and spike shape over the separation in the spike region can be seen in the velocity vector. It is important to mention here that the flow may become severely unsteady under certain conditions[33]. The residual error norms were found oscillating at some time level of iterations on the spike. This is attributed to the flow in the vicinity of the spike containing vorticity of the separation region; therefore, the strict steady-state cannot be obtained in the present numerical simulation. Since these computations do not have time accuracy on account of space variable time-stepping, we are unable to investigate the unsteadiness of the flow. Similar flow field features for the conical spike were observed by Yamauchi et al[16] Number of vortices are observed in the flow separation region, and the velocity magnitude of the flow is low. The flow separation region moves upstream direction as the spike length increased. The bow shock wave, the recirculating zone and the reattachment shock are distinctly visible in the vector plot.

The computed contour plots with schlieren images[34,35] are shown in Fig. 7. These figures depict comparison between the contour plots of the flow field around the hemispherical body with the conical aerospike, the hemispherical aerodisk and the flat-faced aerodisk with L/D = 0·5, 1·0 and 2·0 with the corresponding schlieren pictures. The flowfields are very different between the aerospike of the hemispherical aerodisk, the flat-faced aerodisk and the conical spike as seen in the contour plots. The computed flow fields show agreement with the schlieren photographs. The Mach contours and corresponding vector plots for the flat-face disk, the hemispherical disc and the conical spiked body are shown for Mach 6·0. In Fig. 7(a), and (b), the interaction between the bow shock wave starting from the aero-disc of the spike and the reattachment shock wave of the blunt body is observed. The reflected reattachment wave and shear layer from the interaction are shown behind the reattachment shock wave. A large separated region is observed in front of the blunt body and the shear layer; the boundary of the separated region is clearly seen in Fig. 7. In the aero-disk case as depicted in Figs 7(a) and 7(b), the flow field is characterised by the formation of the bow shock wave in front of the spike, a separated flow region and interaction between the bow shock wave and the reattachment shock wave. The separation region on the spike contributes to reduction in dynamic pressure which is a function of L/D ratio of the spike. The bow shock wave generated from the aerodisk is affected configuration of the spike shape. The body is completely enveloped within the recirculation region, which is separated from the inviscid flow within the bow shock wave by a separation shock. The bow shock wave interacts with the reattachment shock generated by the blunt body. The interaction of the shock wave produced by the hemispherical aerospike differs significantly with the conical spike. The flow separation on the spike and recirculation zone formed on the blunt body cap depends on shape of the spike. The contour plots explain the cause of the drag reduction due to increase of the separation region over the aerodisk type of spike. The normal shock wave in front of the aerodisk will reduce the drag. In the fore region of the aerodisk, the fluid decelerates through the bow shock wave. At the shoulder of the aerodisk or the hemispherical cap, the flow turns and expands rapidly, the boundary layer detaches, forming a free shear layer that separates the inner recirculating flow region behind the base from the outer flow field. The corner expansion over aerodisk process is a modified Prandtl-Mayer pattern distorted by the presence of the approaching boundary layer.

In the case of the conical spike, the conical shock wave is emanated from the tip of the spike as seen in Fig. 7(c) for L/D = 0·5, 1·0 and 2·0. The separated shear layer and the recompression shock from the reattachment point on the shoulder of the hemispherical body are visible. Flow patterns for L/D = 1·0 and 2·0 are similar to that of L/D = 0·5. However, when the spike length is large, the angle of the oblique shock wave from the spike tip decreases, and the flow separation occurs slightly downstream. Because the reattachment point moves aft and the spike is relatively long, the length of the separated region extends. The angle of the conical shock wave depends on the angle of the shear layer, which gives an effective body shape to the outer freestream. Figure 7(c) shows the effects of the L/D ratio on the flow field. The conical shock wave moves further away from the blunted body as compared to L/D = 0·5 and 2·0 and the increase of L/D ratio increases the recirculation zone.

### 5.2 Surface pressure and wall heat flux distribution

The nondimensional surface pressure variations along the spiked blunt body with different spikes and different L/D parameters are illustrated in Figs 8 and 9 using the calculated data. The wall pressure p is nondimensionalised by freestream pressure pa. In Fig. 8, $x/R = 0$ location is from the spike, where R is radius of the blunt body ($R = 0·5D$). The location of the maximum pressure on the surface of the spiked blunt body is at a body angle of about 40°deg for all L/D. The location corresponds to the reattachment point. The
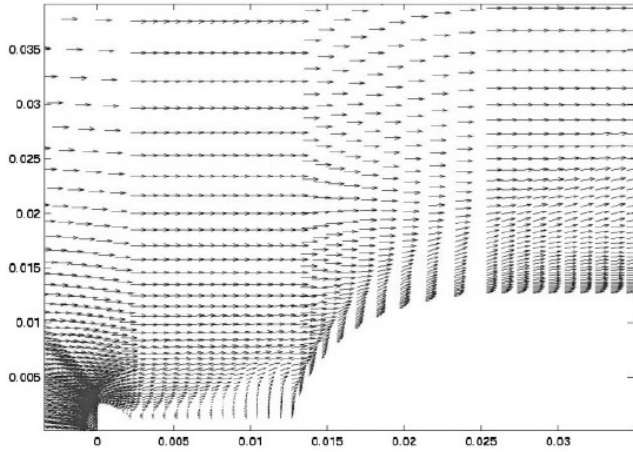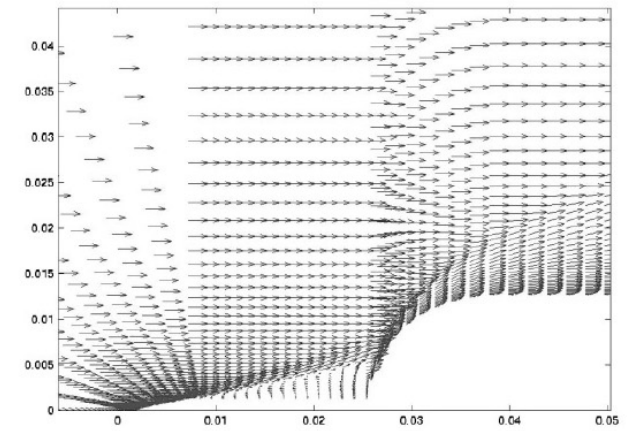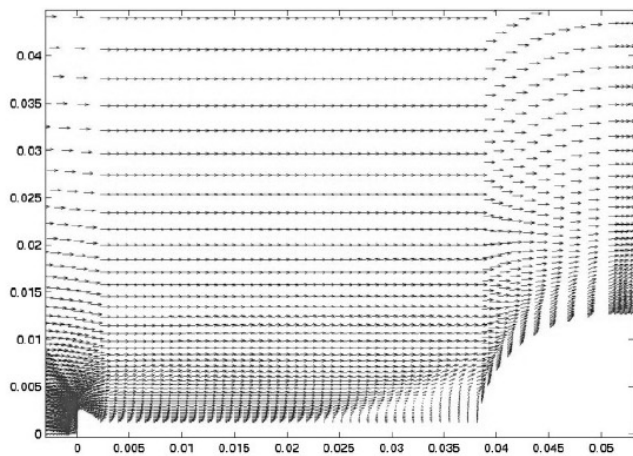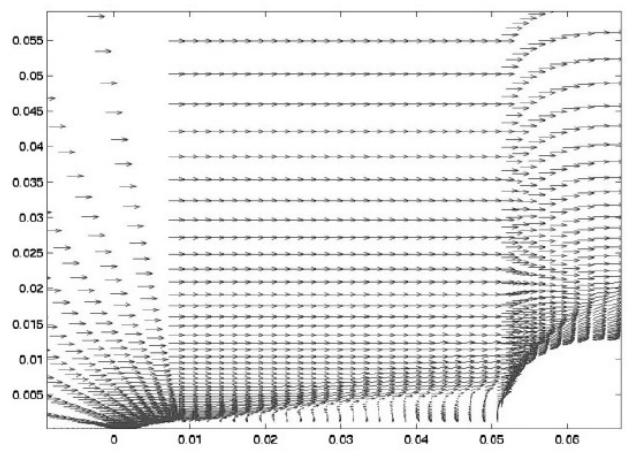
L/D = 0·5
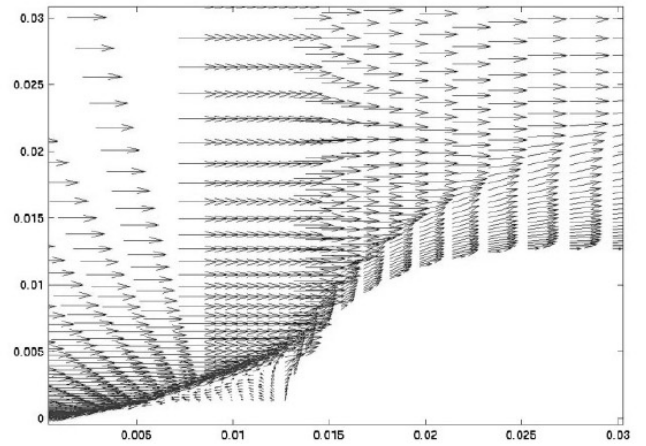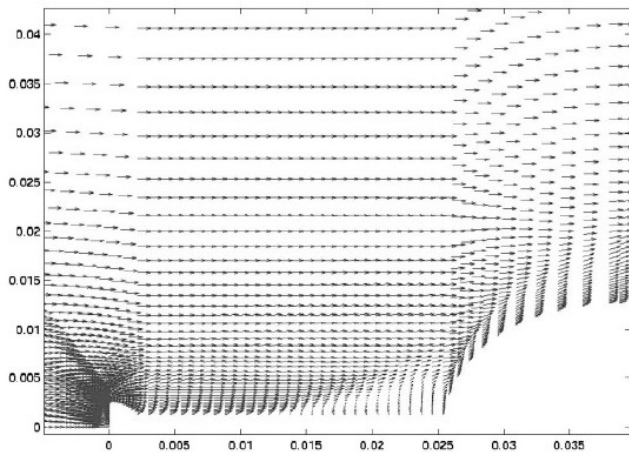
L/D = 1·0

L/D = 2·0

Figure 5. Velocity vector for flat-disk spike.

L/D = 0·5

L/D = 1·0

L/D = 2·0

Figure 6. Velocity vector for conical spike.

L/D = 0·5   *L/D* = 1·0   *L/D* = 2·0

(a) Flat-disk spike

L/D = 0·5   *L/D* = 1·0   *L/D* = 2·0

(a) Hemispherical disk spike

L/D = 0·5   *L/D* = 1·0   *L/D* = 2·0

(c) Conical spike
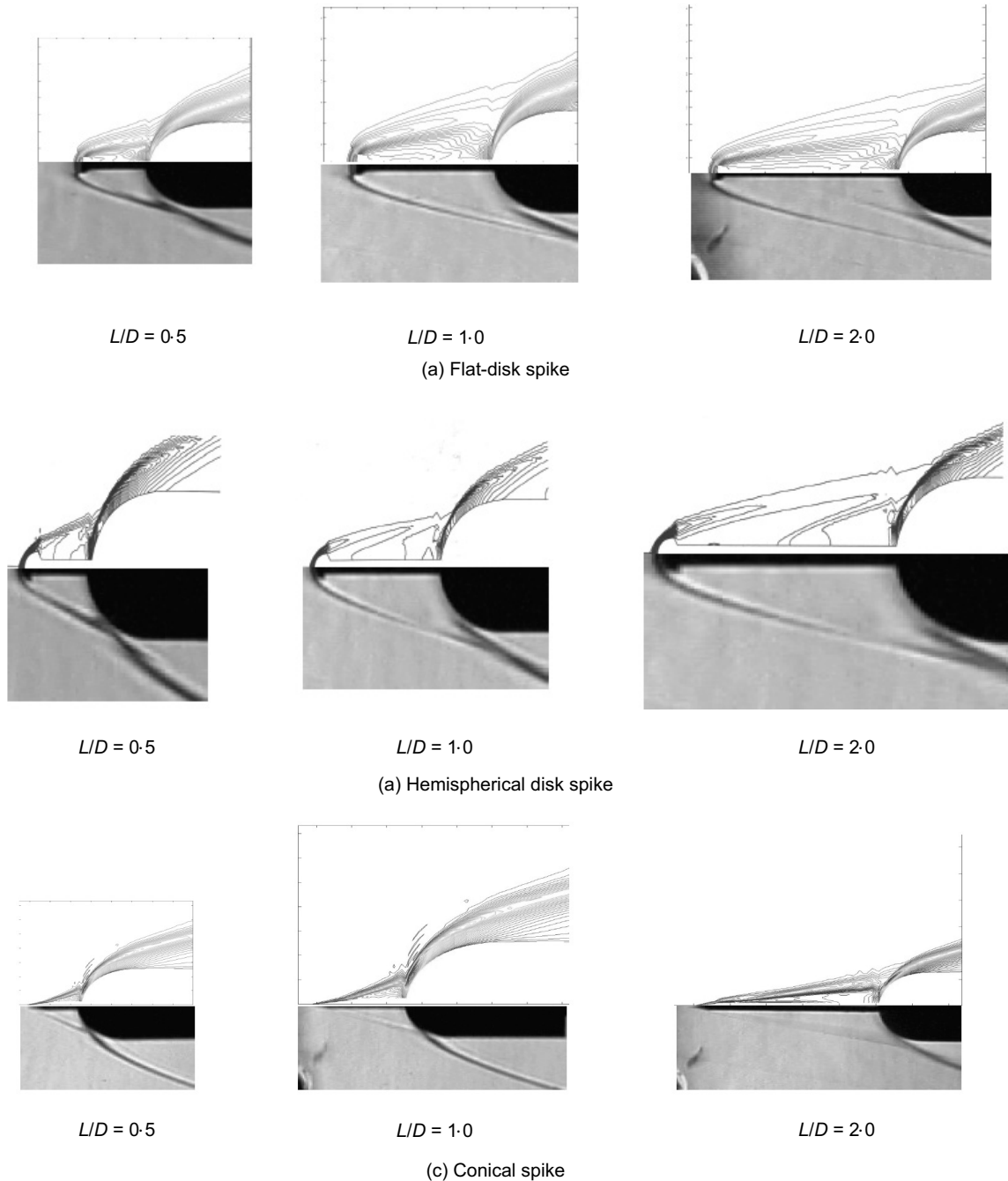
Figure 7. Comparison of contour plots with schlieren images.

maximum as well as the global pressure level decreases when L/D increases. Figures 8(a) and (b) show the pressure variation along the hemispherical and the flat-disk aerospike, respectively, for L/D = 0·5, 1·0 and 1·5. Figure 8(c) depicts the pressure distribution along the conical aerospike for L/D ratios of 0·5, 1·0 and 2·0. The pressure variation shows that the peak pressure falls as the L/D ratio increases. The pressure on the spike is lower as compared to the pressure on the blunt part of the body due to the conical shock wave and the shear layer formed on the spike. The pressure peak on the blunt body decreases with increasing L/D ratios. The pressure rise on the blunt portion is caused by the impinging of the conical shock wave of the spike on the blunt body shock and the resulting reattachment shock. The peak pressure on the blunt body surface reflects the fact that the pressure increases when the shear layer

passes through the reattachment shock wave. Thus, the surface pressure is influenced by the conical shock-reattachment shock inter-action. The pressure distribution on the blunt body is governed by the shear layer created by the shape of the spike, the recirculation region in front of the body, and the resulting shock wave.

The x/R = 0 location is the spike/nose tip junction in Figs 9-12. The relative behaviour of the pressure distribution for various L/D ratios and different spike shapes are shown in Fig. 9(a), (b) and (c). It is interesting to note that the maximum pressure is found on the same location on the blunt body. The pressure on the blunt body is more in the case of the conical spike. The computed value of the ps/pa on the stagnation point of the hemispherical spike and on the flat-face disc spike is about 48·2, which is about 12·5% higher than the analytical value[32] where *ps* is the stagnation point pressure.
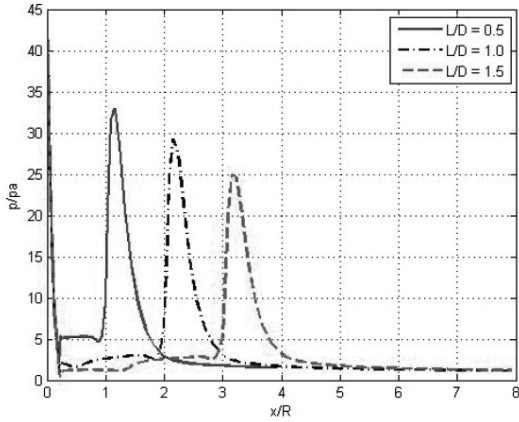
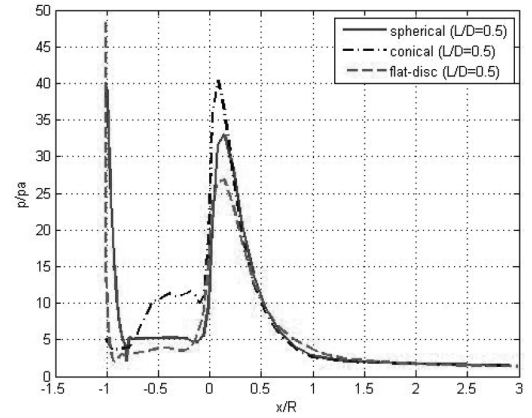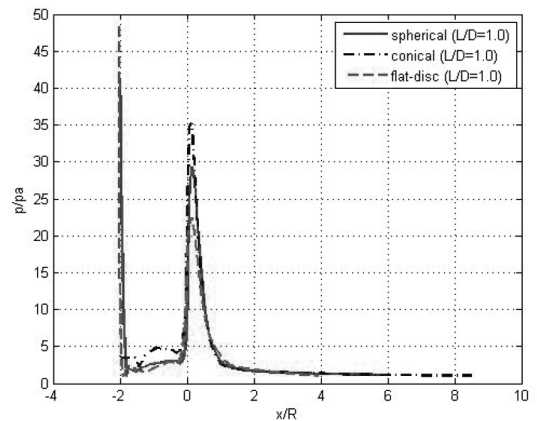(a) Hemispherical spike
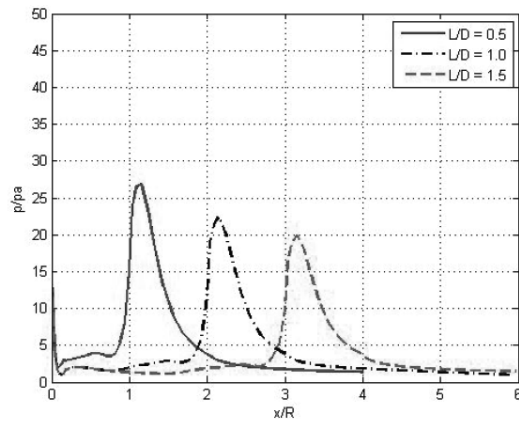
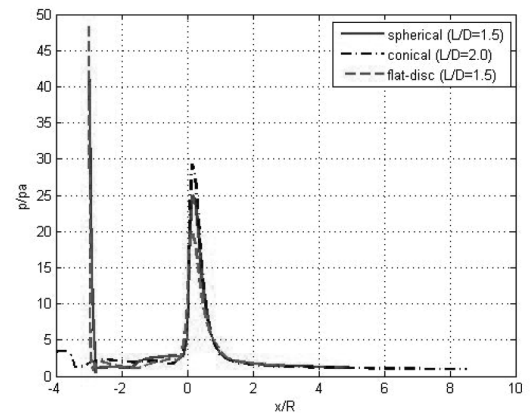(b) Flat disc spike
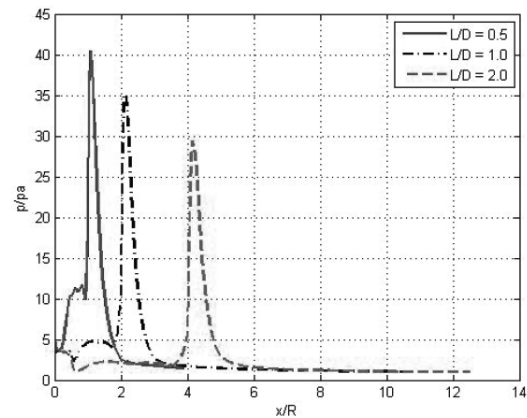
(c) Conical spike

Figure 8. Variation of surface pressure.

(a)

(b)

(c)

Figure 9. Variation of surface pressure.

Figures 10 and 11 show the skin friction variation over the three different types of spikes for different L/D ratios. The numerical simulation gives the effects of the subsonic region over the spike. The present work contains numerical studies for different spike geometries, L/D ratios and a semi-cone angle of 10 deg at Mach 6. Negative skin friction coefficient C_f can be seen on the spike, which is due to the flow separation. The separation zone is found to be function of the spike length and spike configuration. A sharp and sudden rise of C_f is noticed on the spike tip, which is attributed to flow stagnation point. Figure 12 gives the variation of wall heat flux q_w along the spike at different L/D ratio and different spike configurations. The

stagnation point value of the temperature ratio on the hemispherical spike and on the fat-face disc spike is about 13-15% higher than the analytical value[32]. Negative skin friction coefficient can be seen on the spike, which is due to the flow separation. The separation zone is found to be a function of the spike length as well as the shape of the spike. The region of the separation zone can be compared with the velocity vector plots as shown in Figs 4-6. A sharp and sudden rise of skin friction and heat flux is found very close to the conical spike tip, which is attributed to flow stagnation. The secondary peak heat flux is observed about the reattachment point. This secondary peak heat flux decreases with increasing spike length.
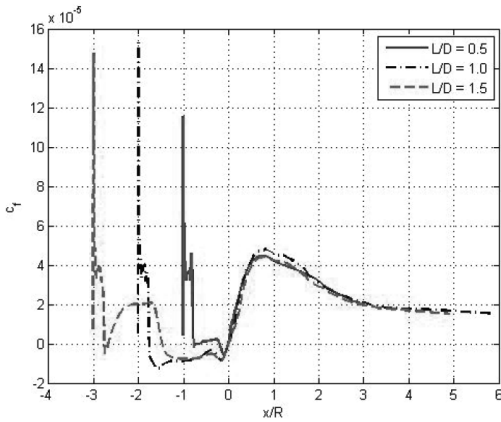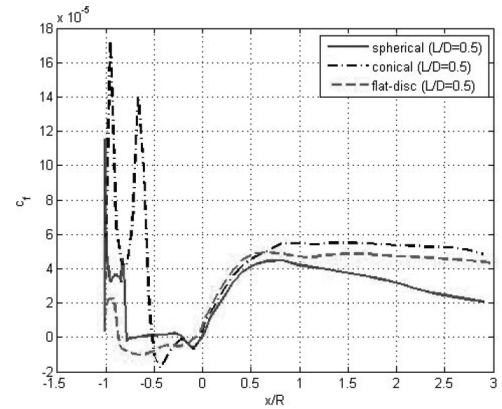
(a) Hemispherical spike
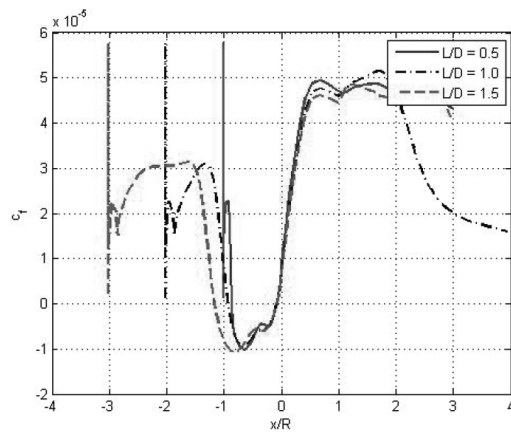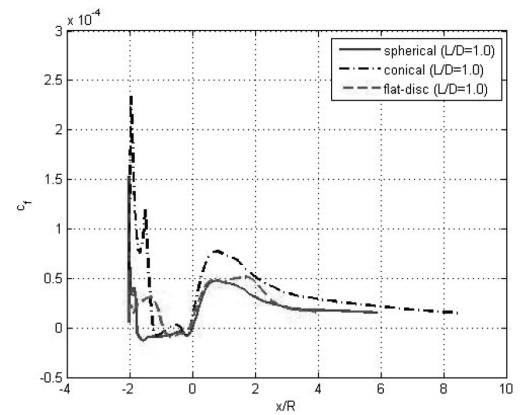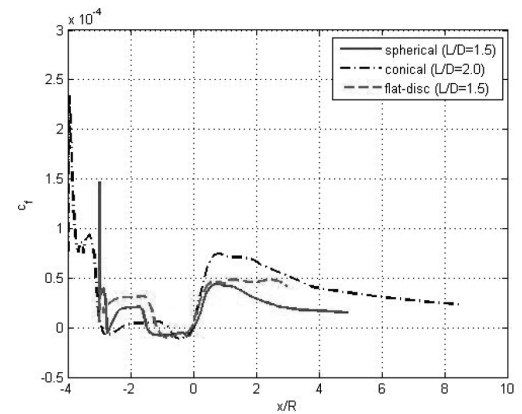

(b) Flat disc spike disc
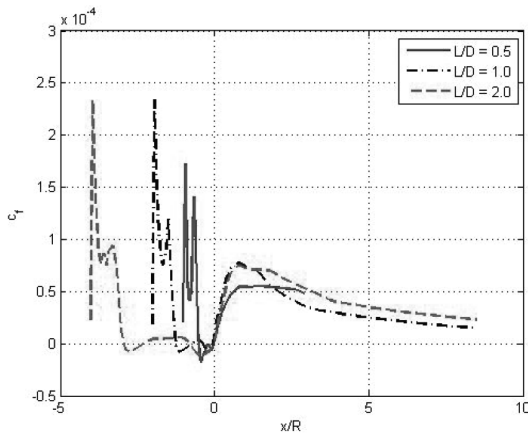
(c) Conical spike

Figure 10. Variation of skin friction coefficient.

(a)

(b)

(c)

Figure 11. Variation of skin friction coefficient.

5.3 Pressure drag

The contour plots reveal the flow field behavior over the spike and also the drag reduction mechanism due to interaction of the shock waves, which is influenced by the spike configurations as observed in the velocity vector plots. As the spike nose becomes large from a conical nose to a flat-faced nose, the total pressure drag decreases.

The effects of the geometrical parameters on the aerodynamic drag are investigated. The flow field was computed for $M = 6$ and for $L/D = 0.5$, 1.0 and 2.0. The main purpose of the numerical simulation is to find out the effects of the subsonic region over the spike. The diag coefficient is calculated as:

$$C_D = \frac{\int_S F_x dS}{\frac{1}{2}\rho_\infty V_\infty^2 S_0} \qquad \ldots (8)$$

where F_x is the axial pressure component, dS is the area of the segment and reference surface area is $S_0 = 0.25\pi D^2$. The aerodynamic drag is computed for different spike geometries, L/D ratio and semi-cone angle at Mach 6. As the curvature radius of the spike nose becomes large from a conical nose to a flat-faced nose, the total pressure drag decreases. From the flow field point of view, the
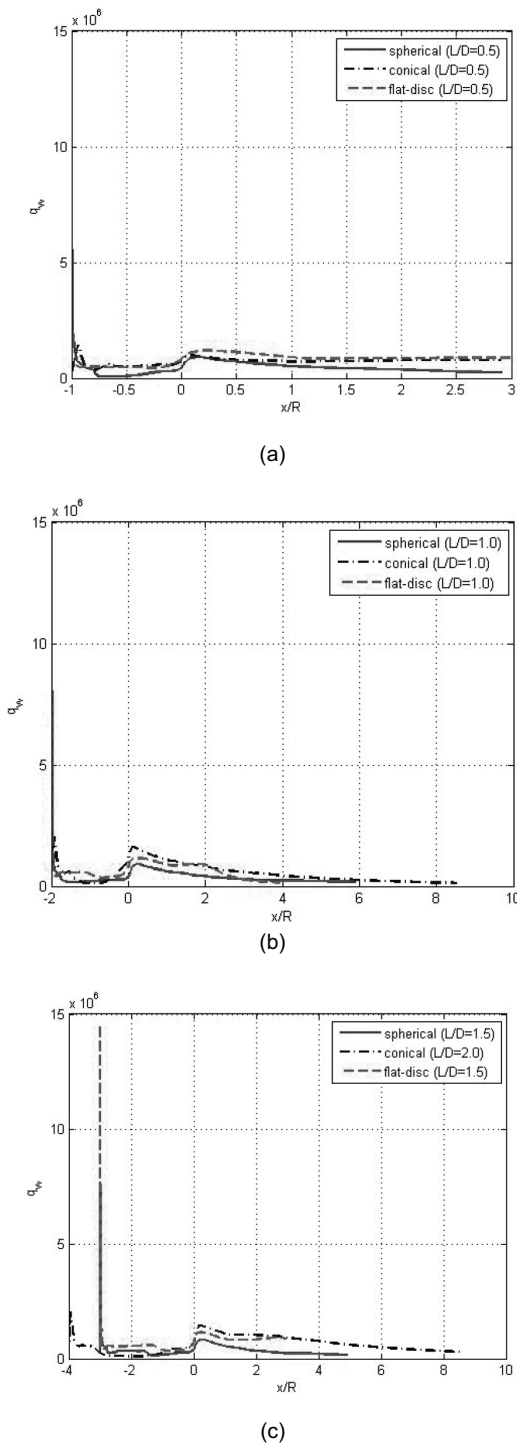
(a)

(b)

(c)

Figure 12. Variation of wall heat flux.

aerodisk with $L/D = 2\cdot0$ has the potential for the greatest drag reduction in this computational result. Motoyama *et al*[15] also experimentally observed through the flow visualisation technique at Mach 7 that a bow shock wave is generated ahead of the aerodisk, and a large recirculating zone enveloped the aerospike. The maximum C_D difference between the numerical results[30] and the experimental data of Crawford[14] at M = $6\cdot8$ and $L/D = 2\cdot0$ is found to about 20%. The accuracy of the measurement data is not available. It was found by them that the aerodisk spike has shown a better drag reduction capability in comparison to the other types of aerospike configurations. Table 1 gives the computed value of the drag coefficient for

the three different spike configurations. The comparisons of the drag on each of the spiked blunt body configuration (the conical, the hemispherical-disk and the flat-face) can be observed. It is important to note that the spike is advantageous for drag reduction. This is also noticed in the above flow field visualisations. The drag on a conical spiked blunt body is smaller than that on a blunt body without the spike. As expected, the drag of the blunt body is remarkably influenced by the spike length and spike shape. Thus, the drag is reduced because of the existence of the separated region created by the spike on the nose. The separated flow at the nose is extended with an increase in the spike length. The computed values of C_D are compared with the experimental results of Ref. 34 and are found in an agreement. The key feature of the drag reduction is the pressure distribution on the body surface, particularly near the forward facing spike attached to the blunt body. As expected, the drag of the blunt body is significantly influenced by the spike length.

Table 1
Aerodynamic Drag over the Aerospike

Spike geometry	$L/D = 0\cdot5$	$L/D = 1\cdot0$	$L/D = 2\cdot0$
Conical aerospike	$0\cdot868$	$0\cdot582$	$0\cdot384$
Hemisphere aerodisk	$0\cdot576$	$0\cdot317$	$0\cdot231$
Flat face aerodisk	$0\cdot458$	$0\cdot309$	$0\cdot277$

6.0 CONCLUSION

The paper has treated numerically the influence of various shapes of spikes mounted on a hemispherical nose of a blunt body at a free stream Mach number 6. The numerical simulations were carried out using finite volume method, and for the flat disk spike, the hemispherical disk spike and the conical spike and length to diameter ratios at zero angle-of-attack. To explain the influence of the shape of the spike and length to diameter ratios, flow field visualisation were performed using the velocity vector and contour plots. The computed contours agree well with the schlieren pictures of the experiments. The bow shock wave formation is found over the spherical and the flat disc spike which gives different separation zone in the vicinity of the spiked blunt body. The conical shock wave is emanating from the conical spike tip and impinges on the blunt body. Thus, the flow field, immediately behind the aero-disk spike shows a complex flow field due to aero-disk geometry as compared to the conical spike. The aerodynamic drag of the blunt body is remarkably influenced by the spike length and the spike shape. The formation of the shock wave over the spike and the reattachment point of the shear layer on the blunt body can be used for a suitable geometrical configuration of the spike nose.

ACKNOWLEDGEMENT

REFERENCES

1. Riggins, D., Nelson, H.F. and Johnson, E. Blunt body wave drag reduction using focused energy deposition, *AIAA J*, 1999, **27**, pp 460-467.
2. Kobayashi, H., Maru, Y. and Fukiba, K. Experimental study on aerodynamic characteristics of telescopic aerospikes with multiple disks, *J Spacecraft and Rockets*, 2007, **44**, (1), pp 33-41.
3. Bogdonoff, S.M. and Vas, I.E. Preliminary investigations of spike bodies at hypersonic speeds, *J Aerospace Sciences*, February 1959, **26**, (2), pp 65-74.
4. Maull, D.J. Hypersonic flow over symmetric spiked bodies, *J Fluid Mechanics*, 1960, **8**, (584).

5. WOOD, C.J. Hypersonic flow over spiked cones, *J Fluid Mechanics*, 1961, **12**, (614).

6. MENEZES, V., SARAVANAN, S., JAGDEESH, G. and REDDY, K.P. Experimental investigation of hypersonic flow over highly blunted cones with aerospikes, *AIAA J*, 2003, **41**, (10), pp 1955-1966.

7. MEHTA, R.C. Pressure oscillations over a spiked blunt body at hypersonic Mach number, *Computational Fluid Dynamics J*, July 2000, **9**, (2), pp 88-95.

8. MEHTA, R.C. Numerical analysis of pressure oscillations over axisymmetric spiked blunt bodies at Mach 6·8, *Shock Waves*, 2002, **11**, pp 431-440.

9. MILICV, S.S., PAVLOVIC, M.D., RISTIC, S. and VITIC, A. On the influence of spike shape at supersonic flow past blunt bodies, *Faculty Universities, Series: Mechanics, Automatic Control and Robotic*, 2002, **3**, (12), pp 371-382.

10. CAARESE, W. AND HANKEY, W.L. Modes of shock wave oscillations on spike tipped bodies, *AIAA J*, **23**, (2), 1985, pp 185-192.

11. HAHN, M. Pressure distribution and mass injection effects in the transitional separated flow over a spiked body at supersonic speed, *J Fluid Mechanics*, February 1966, **24**, part 2, pp 209-223.

12. MILICEV, S.S. and PAVLOVIC, M.D. Influence of spike shape at supersonic flow past blunt nosed bodies experimental study, *AIAA J*, 2002, **40**, (5), pp 1018-1020.

13. KUBOTA, H. Some aerodynamic and aerothermodynamic considerations for reusable launch vehicles, AIAA-2004-2428.

14. CRAWFORD, D.H. Investigation of the flow over a spiked-nose hemisphere at a Mach number of 6·8, NASA TN-D 118, December 1959.

15. MOTOYAMA, N., MIHARA, K., MIYAJIMA, R., WATANUKI, W. and KUBOTA, H. Thermal protection and drag reduction with use of spike in hypersonic flow, AIAA Paper 2001-1828, 2001.

16. YAMAUCHI, M., FUJJII, K., TAMURA, Y. and HIGASHINO, F. Numerical investigation of hypersonic flow around a spiked blunt body, AIAA paper 93-0887, January 1993.

17. SHOEMAKER J.M. Aerodynamic spike flowfields computed to select optimum configuration at Mach 2·5 with experimental validation, AIAA Paper 90-0414, 1990.

18. FUJITA, M. and KUBOTA, H. Numerical simulation of flowfield over a spiked blunt nose, *Computational Fluid Dynamics J*, 1992, **1**, (2), pp 187-195.

19. BOYCE, R., NEELY, A., ODAM, J. and STEWART, B. CFD Analysis of the HyCAUSE Nose-Cone, AIAA Paper 2005-3339, May 2005.

20. MILICEV, S.S., PAVLOVIC, M.D., RISTIC, S. and VITIC, A. On the influence of spike shape at supersonic flow past blunt bodies, *Mechanics, Automatic Control and Robotics*, 2002, **3**, (12), pp 371-382.

21. MEHTA, R.C. Peak heating for reattachment of separated flow on a spiked blunt body, *Heat and Mass Transfer*, 2000, **36**, pp 277-283.

22. MEHTA, R.C. and JAYACHANDRAN, T. Navier-Stokes solution for a heat shield with and without a forward facing spike, *Computers and Fluids*, 1997, **26**, (7), pp 741-754.

23. MEHTA, R.C. Heat transfer study of high speed over a spiked blunt body, *Int J Numerical Methods for Heat & Fluid Flow*, 2000, **10**, (7), pp 750 – 769.

24. GAUER, M. and PAULL, A. Numerical investigation of a spiked nose cone at hypersonic speeds, *J Spacecraft and Rockets*, 2008, **45**, (3), pp 459-471.

25. PEYRET, R. and VIVIND, H. *Computational Methods for Fluid Flows*, Springer-Verlag, 1993, Berlin, Germany, pp 109-111.

26. JAMESON, A., SCHMIDT, W. and TURKEL, E. Numerical simulation of Euler equations by finite volume methods using Runge-Kutta Time Stepping Schemes, AIAA paper 81-1259, June 1981.

27. MEHTA, R.C. Numerical investigation of viscous flow over a hemisphere-cylinder, *Acta Mechanica*, 1998, **128**, (1-2), pp 48-58.

28. SHANG, J.S. Numerical simulation of wing-fuselage aerodynamic interference, *AIAA J*, 1984, **22**, (10), pp 1345-1353.

29. MEHTA, R.C. A quasi-three dimensional automatic grid generation method, in the proceedings of the 25th National & International Conference on Fluid Dynamics & Fluid Power, Indian Institute of Technology, Delhi, India, December 1998, pp 89-98.

30. MEHTA, R.C. Numerical heat transfer study over spiked-blunt body at Mach 6.8, AIAA Paper 2000-0344, January 2000 and also *J Spacecraft & Rockets*, 2000, **37**, (5), pp 700 – 701.

31. TRUITT, R.W. *Hypersonic Aerodynamic*, The Ronald Press Co, New York, USA, 1959.

32. LIEPMANN, H.W. and ROSHKO, A. *Elements of Gas Dynamics*, 2007, Dover Publications Inc, First South Asian Edition, New Delhi, India.

33. MAIR, W.A. Experiments on separation on boundary layers on probes in front of blunt bodies at supersonic air stream, *Philosophical Magazine*, 1952, **43**, pp 695-716.

34. KALIMUTHU, R., MEHTA, R.C. and RATHAKRISHNAN, E. Experimental Investigation on spiked body in hypersonic flow, *Aeronaut J*, October 2008, **112**, (1136), pp 593-598.

35. KALIMUTHU, R., MEHTA, R.C. and RATHAKRISHNAN, E. Blunt body drag reduction using aero-spike and aero-disk at Mach 6, in the proceedings of International Conference on High Speed Trans-atmospheric Air & Space Transportation, Hyderabad, India, June 2007, pp 178-188.